The True Structure of Hexagonal Mesophase-Templated Silica Films As Revealed by X-ray Scattering: Effects of Thermal Treatments and of Nanoparticle Seeding

Michaela Klotz,[†] Pierre-Antoine Albouy,[‡] André Ayral,*[,†] Christine Ménager,[§] David Grosso,[||] Arie Van der Lee,[†] Valérie Cabuil,[§] Florence Babonneau,[||] and Christian Guizard[†]

Laboratoire des Matériaux et Procédés Membranaires, UMR 5635, CNRS, ENSCM, UMII, 8, rue de l'Ecole Normale, 34296 Montpellier Cedex 5, France; Laboratoire de Physique des Solides, UMR CNRS 8502 Université de Paris-Sud, 91405 Orsay, France; Laboratoire Liquides Ioniques et Interfaces Chargées, UMR CNRS 7612, Université P. et M. Curie, 4, place Jussieu, 75252 Paris Cedex, France; and Laboratoire de Chimie de la Matière Condensée, UMR CNRS 7574, Université P. et M. Curie, 4, place Jussieu, 75252 Paris Cedex, France

Received December 28, 1999. Revised Manuscript Received March 13, 2000

This work describes the detailed structural investigation of mesophase-templated mesoporous silica films by 1D and 2D X-ray scattering techniques and transmission electron microscopy. The films are prepared by sol−gel dip coating with 2D hexagonal templating mesophases, yielding 2D mesoporous structures consisting of cylindrical pores whose axes are aligned parallel to the surface. It is shown that drying and thermal treatments induce an unidirectional shrinkage of the layers in the direction of the normal of the film. The true rectangular symmetry is only evidenced by 2D X-ray scattering in two different scattering geometries. 1D diffraction gives only an apparent hexagonal symmetry. It is furthermore shown that although the cylinder axes are randomly orientated within the plane parallel to the surface, there are large domains with well aligned 2D planar unit cells perpendicular to the surface. It is demonstrated that this preferential ordering is destroyed by nanoparticle seeding with amorphous silica or maghemite particles.

Introduction

Since the pioneering work of Beck et al.[1,2] on the hydrothermal synthesis of aluminosilicates with an ordered porosity obtained by the templating effect of lyotropic liquid crystals, much work has been devoted to mesophase-templated mesoporous materials. These studies concerned new ways of synthesis involving room temperature and atmospheric pressure conditions or the use of nonionic or block copolymers surfactants. A number of studies dealt with the preparation of sol−gel-derived supported silica thin layers.[3−9] In particular, 2D hexagonal mesophases are interesting for templating ordered porous silica layers, because they have a very large domain of formation. A recent study[10] showed that the synthesis conditions for crack-free silica thin layers prepared from ionic alkyltrimethylammonium bromides surfactants could be predicted from the corresponding water−surfactant binary diagrams. Nonionic surfactants such as the triblock copolymer Pluronic F127 (viz. $OH(CH_2CH_2O)_{106}(CHCH_3CH_2O)_{70}(CH_2CH_2O)_{106}H$) can be equally well used as a templating agent for the preparation of 2D mesoporous silica films.[11]

One of the first techniques to be used for the characterization of these micelle-templated structures is X-ray diffractometry. With X-ray diffraction the ordering of the pores and the pore-to-pore distance can be easily detected. Usually classical 1D X-ray diffraction in Bragg−Brentano geometry is performed, i.e., only lattice planes parallel to the surface are detected, and the detector is moved in only one scattering plane, perpendicular to the surface. Although this is a perfect setup

* To whom correspondence should be addressed. E-mail: ayral@cit.enscm.fr. Phone: 33 4 67 14 72 31. Fax: 33 4 67 14 43 47.
[†] Laboratoire des Matériaux et Procédés Membranaires.
[‡] Laboratoire de Physique des Solides.
[§] Laboratoire Liquides Ioniques et Interfaces Chargées.
[||] Laboratoire de Chimie de la Matière Condensée.

(1) Kresge, C. T.; Leonowicz, M. E.; Roth, W. J.; Vartuli J. C.; Beck, J. S. *Nature* **1992**, *359*, 710.
(2) Beck, J. S.; Vartuli, J. C.; Roth, W. J.; Leonowicz, M. E.; Kresge, C. T.; Schmitt, K. D.; Chu, C. T.-W.; Olson, D. H.; Sheppard, E. W.; McCullen, S. B.; Higgins, J. B.; Schlenker, J. L. *J. Am. Chem. Soc.* **1992**, *114*, 10834.
(3) Ogawa, M. *J. Am. Chem. Soc.* **1994**, *116*, 7941.
(4) Dabadie, T.; Ayral, A.; Guizard, C.; Cot, L.; Lacan, P. *J. Mater. Chem.* **1996**, *6*, 1789.
(5) Ogawa, M. *Chem. Commun.* **1996**, 1149.
(6) Bruinsma, P. J.; Hess, N. J.; Bontha, J. R.; Liu, J.; Baskaran, S. *Mater. Res. Soc. Symp. Proc.* **1997**, *443*, 105.
(7) Lu, Y.; Ganguli, R.; Drewien, C. A.; Anderson, M. T.; Brinker, C. J.; Gong, W.; Guo, Y.; Soyez, H.; Dunn, B.; Huang, M. H.; Zinks, J. I. *Nature* **1997**, *389*, 364.
(8) Martin, J. E.; Anderson, M. T.; Odinek, J.; Newcomer, P. *Langmuir* **1997**, *13*, 4133.
(9) Zhao, D.; Yang, P.; Melosh, N.; Feng, J.; Chmelka, B. F.; Stucky, G. D. *Adv. Mater.* **1998**, *10*, 1380.
(10) Klotz, M.; Ayral, A.; Guizard, C.; Cot. *J. Mater. Chem.***2000**, *10*, 663.
(11) Grosso, D.; Balkenende, A. R.; Albouy, P. A.; Babonneau, F. Proceeding of the 2nd Conference on the Access in Nanoporous Materials, Banff, Canada, 2000, submitted for publication.

10.1021/cm991198t CCC: $19.00
Published on Web 05/16/2000

for a powder with randomly oriented crystallites, it is much less suitable for the structural characterization of 2D mesoporous materials, which are normally highly textured. Moreover 2D X-ray scattering was efficiently applied to characterize the orientation of mesophase-templated monoliths.[12]

We show in this paper how the use of an image plate system coupled to two different scattering geometries can reveal the true symmetry of 2D thermally treated silica films, a symmetry that is overlooked when classical 1D X-ray diffraction is employed. Finally the effect of seeding by nanoparticles on the texture of the resulting layers is investigated.

Experimental Section

Synthesis. *CTAB-Based Samples (Labeled C).* The exact conditions for the synthesis of 2D mesoporous silica films from tetramethoxysilane or tetraethoxysilane and different alkyltrimethylammonium bromides have been described elsewhere.[10] In the present work only one chemical composition is considered: tetraethoxysilane: ($Si(OC_2H_5)_4$ (TEOS), purity > 98%), acidic water (pH = 2; HCl added), ethanol, and cetyltrimethylammonium bromide ($C_{16}H_{33}(CH_3)_3N^+,Br^-$ (CTAB), purity > 98%) with the following molar ratios: 1:8.2:3.5:0.14. This composition gives rise to phases with a maximal diffracted intensity.[10] The synthesis is carried out in two steps: Alkoxide, ethanol, and one-half of the water are first mixed. After an aging time of 1 h, the second half of the water and the surfactant are added. After two additional hours of aging the solution is deposited on the substrates (see below).

For nanoparticle seeding two kinds of colloidal particles are used: maghemite (γ-Fe_2O_3) particles with a particle diameter equal to 7 nm (synthesized as described in ref 13) and amorphous silica particles with a particle size equal to 12 nm (from commercial sol Ludox HS40, Du Pont). They are introduced as diluted sols adjusted at pH = 2 in place of the second added volume of water. The volume fractions in the sols are 1% and 4.4% for maghemite and silica, respectively. These volume fractions correspond to a seed density of one nanoparticle per 25 nm-size cube in the final film. The corresponding volume fractions in the final layers are 1.4% and 5.5% for maghemite and silica seeded layers, respectively.

The sols are deposited by dip coating (withdrawal rate: 5 cm min^{-1}) on two different flat substrates: thick slides of soda lime−silica glass and thin silicon wafers (thickness: 10 μm) polished on each side (VA 22401 provided by Virginia Semiconductor Inc., Fredericksburg, MD). The single-crystal Si substrates combine a low X-ray absorbance (1/e attenuation length at normal incidence 72 μm) with a reduced background scattering, so that the recorded X-ray scattering pattern is not greatly affected by the presence of the substrate.[14]

The samples are first dried at 20 °C during 12 h and next for 2 h at 100, 150, and 175 °C in an oven. The thermal treatment inducing the departure of the surfactant is carried out under nitrogen at 450 °C for 1 h.

Pluronic-Based Sample (Labeled P). A prehydrolyzed solution of TEOS is prepared by refluxing for 1 h a solution composed of TEOS, EtOH, HCl, and H_2O (molar ratios: 1:3:5 × 10^{-5}:1 respectively). Separately, the Pluronic F127 surfactant (poly(ethylene oxide)−poly(propylene oxide), purchased from BASF) is dissolved in an ethanolic solution containing additional amounts of water and hydrochloric acid. The two solutions are then mixed together and stirred for 24 h at room temperature. The amount of ethanol, water, and hydrochloric acid in the second solution are adjusted as to obtain the typical following molar ratios in the final solution ($TEOS/EtOH/HCl/H_2O$/F127, 1:20:0.004:5:0.005). The dip coating withdrawal rate is adjusted at 19 cm min^{-1}. The film is subsequently dried overnight in air and finally undergoes the thermal treatment for 1 h at 350 °C.

Characterization. The ordered structure of the layers is investigated with a BRUKER D5000 diffractometer using Cu K $L_{3,2}$ radiation, monochromatized by a graphite crystal in the diffracted beam. The peak evolution versus thermal treatment temperature is followed in $\theta/2\theta$ Bragg−Brentano scattering geometry, 2θ varying from 1.2 to 9°. The texture of the layers is analyzed in a fixed incidence angle mode (detector scan). For fixed incidence angles α (angle between incident beam and sample surface) ranging from 0.025 and 5°, the detector rotates between 1.5 and 3.5° in 2θ (angle between incident and diffracted beam).

Two-dimensional (2D) X-ray scattering analyses are performed with a rotating anode X-ray generator (copper anode operated at 50 kV, 30 mA; small focus) equipped with two different optical systems: (i) a doubly curved graphite monochromator delivering an intense beam with a limited resolution (maximal accessible *d* spacing: ∼8 nm); and (ii) a double-focusing optical system consisting of a parabolic graded multilayer monochromator and a bent nickel-coated glass mirror. The beam quality is in the second case markedly improved while keeping satisfactory flux (maximal accessible *d* spacing: ∼20 nm). The sample can be freely rotated around a vertical axis and the sample-to-detector distance, l_{sd}, is continuously adjustable. A vacuum pipe reduces the air scattering. The scattering is recorded on photostimulable imaging plates. The exposure time, t_e, is ranging from 14 min to 15 h. In addition to the two optical systems, two different scattering geometries were used: a normal beam configuration giving access to in-plane preferential orientations and a grazing incident geometry which reveals the out-of-the-plane organization. In the latter geometry the incident angle is varied between −7° and +7°. Reciprocal positions are systematically translated into the corresponding *d* spacing value, using the relation $q = 2\pi/d$.

Transmission electron microscopy (TEM, JEOL 100CX2) is done on microtomed slides (thickness 70 nm) of samples embedded in a polymer resin.

Results and Discussion

Texture and Thermal Evolution of the Crystalline Structure for Unseeded Thin Layers. *CTAB-Based Samples.* Figure 1 shows the 1D classical X-ray patterns for unseeded thin layers as a function of

(12) Tolbert, S. H.; Firouzi, A.; Stucky, G. D.; Chmelka, B. F. *Science* **1997**, *278*, 264.
(13) Massart, R. *IEEE Trans. Magn. Magn. Magn.* **1981**, *17*, 1247.
(14) Albouy, P.-A. *J. Phys. Chem.* **1994**, *98*, 8543.

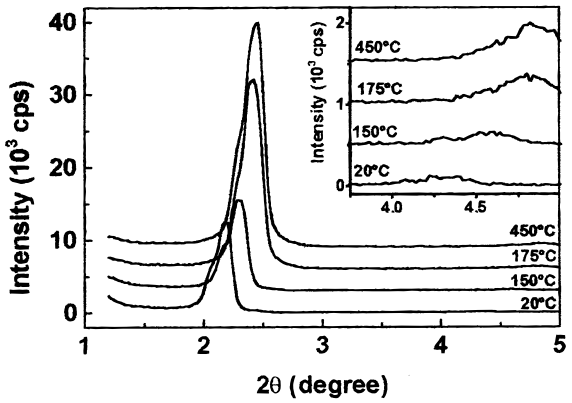

Figure 1. 1D classical X-ray diffraction: evolution of the diffraction pattern as a function of the thermal treatment temperature for unseeded thin layer C.

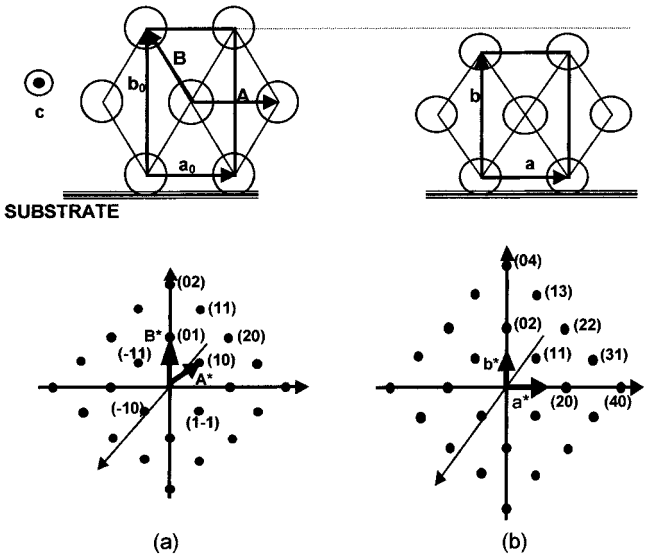

Figure 2. Schematic representation of the real and reciprocal lattices and corresponding indexing for two bidimensional structures: (a) hexagonal and (b) centered rectangle.

thermal treatment temperature. The main diffraction peak for the sample dried at 20 °C is located at $d_{20\ °C}$ = 4.04 nm, and corresponds to the planes (01) assuming a 2D hexagonal structure (Figure 2a). When the drying temperature increases to 175 °C, a shift of the peak is observed: $d_{175\ °C}$ = 3.64 nm. The evolution of the Bragg spacing from 175 to 450 °C is lower: $d_{450\ °C}$ = 3.58 nm. The peak width does not vary significantly with temperature. The calculated size of the ordered domains is around 100 nm. The diffracted intensity is strongly dependent on the temperature (Figure 1). A strong increase is observed between 150 and 175 °C prior to the departure of the surfactant. This was previously assigned to an increase of the contrast in electronic density between walls and pores, associated with the departure of the residual water.[10] In addition to the main peak, d_{01}, only one peak, d_{02}, with a very low intensity, can be observed. The fact that only these two peaks are visible can be explained by an alignment of the micellar cylinders parallel to the substrate plane. Other diffracting planes than those parallel to the surface cannot be observed in Bragg−Brentano scattering geometry. Previous studies[15,16] have evidenced the role of both the solid−solution and air−solution interfaces in the formation of 2D hexagonal mesophases

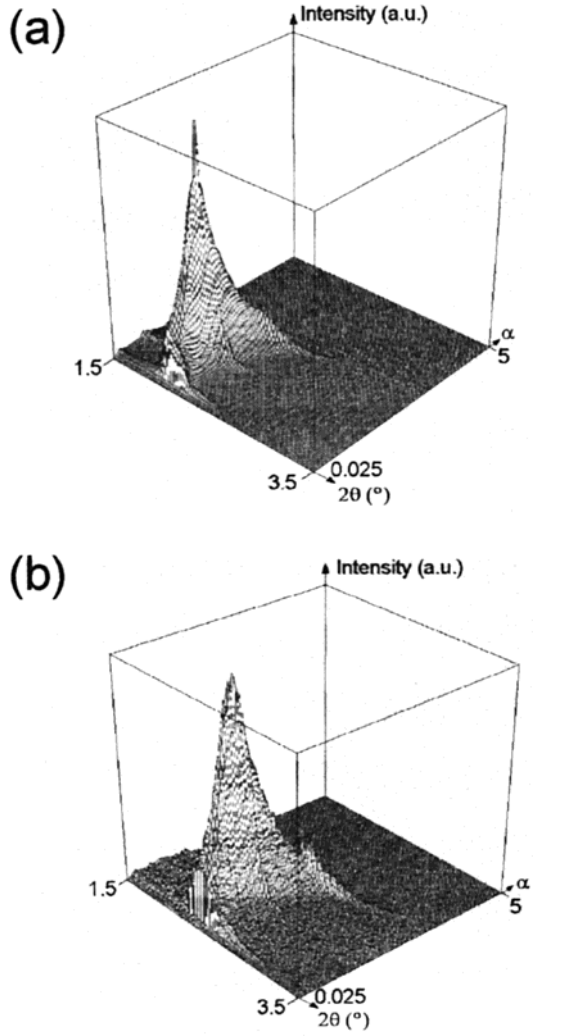

Figure 3. 1D classical X-ray diffraction as a function of incidence angle α for unseeded thin layers C: (a) 20 °C and (b) 450 °C.

and their alignment parallel to these interfaces. Figure 3a and 3b show the variations of the diffracted intensity I_{01} versus the incidence angle α and 2θ for a layer dried at 20 °C and a layer thermally treated up to 450 °C. In each case a strong maximum is observed for $\alpha = \theta_{01}$, corresponding to the expected diffraction angle for planes (01) parallel to the substrate surface. The excellent alignment of the cylindrical pores parallel to the surface is confirmed by transmission electron microscopy observations (Figure 4).

The 2D scattering patterns are shown in Figure 5. The relevant structural parameters obtained with the CTAB-based samples in both scattering geometries are gathered in Tables 1 and 2. The pattern for the layer dried at 20 °C (Figure 5a) is taken in normal beam geometry and reveals two homogeneous rings located at 4.89 and 2.79 nm. It can be noticed that these positions are in the ratio 1.75, close to $\sqrt{3}$. The second patterns (Figure 5b) are taken at grazing incidence and two different scattering features can be distinguished: the first one consists of well-defined diffraction spots

(15) Yang, H.; Kuperman, N.; Coombs, N.; Mamiche-Afara, S.; Ozin, G. A. *Nature* **1996**, *379*, 703.
(16) Yang, H.; Coombs, N.; Sokolov, I.; Ozin, G. A. *Nature* **1996**, *381*, 589.

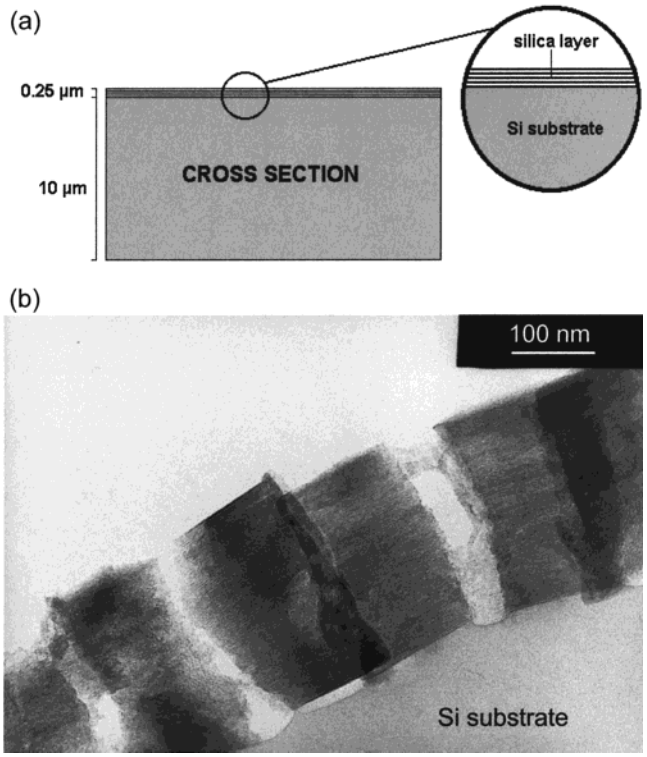

Figure 4. TEM cross section observation of a calcined unseeded thin layer C: (a) schematic representation of the observed section and (b) TEM image.

whose positions can be indexed using a centered rectangular cell of parameters $a = 5.58$ nm and $b = 8.06$ nm (Figure 2b, planar space group $c2mm$). When comparing Figure 5a and Figure 5b, one notices that the (2 0) spot originates from the intersection of the Ewald sphere of reflection with the outer scattering ring ($d = 2.79$ nm; Figure 5a) when turned by 90°. In other words, the corresponding scattering object in reciprocal space must be a circle parallel to the surface and centered onto the origin. Similarly it is possible to show by recording scattering patterns at intermediate incident angles that any observed (h k) spot arises from the intersection of a circle parallel to the surface and the Ewald sphere. This point will be discussed in detail below. The second scattering feature is a diffuse ellipse with short and long axes of 4.03 and 4.89 nm, respectively (black arrow). This last value corresponds to the d spacing of the inner ring observed in Figure 5a. For the small angles presently considered, the relevant section of the Ewald sphere surface may be approximated by a plane: in this condition X-ray patterns corresponding to different incidence angles are images of sections of the reciprocal space for these angles. It follows that the real 3D diffracting object is an ellipsoid with revolution symmetry around the normal to the substrate. An additional feature that can be noticed is a horizontal diffusion streak indicated by the grey arrow. It is merely due to the specular reflection of the beam on each side of the substrate.

The layer calcined at 450 °C displays similar X-ray scattering features as the layer dried at 20 °C (Figure 5c). However there are fewer diffraction spots and they are weaker in intensity. This is in contrast with what is observed using classical 1D diffraction (Figure 1). It is noted that the analyzed samples are not the same

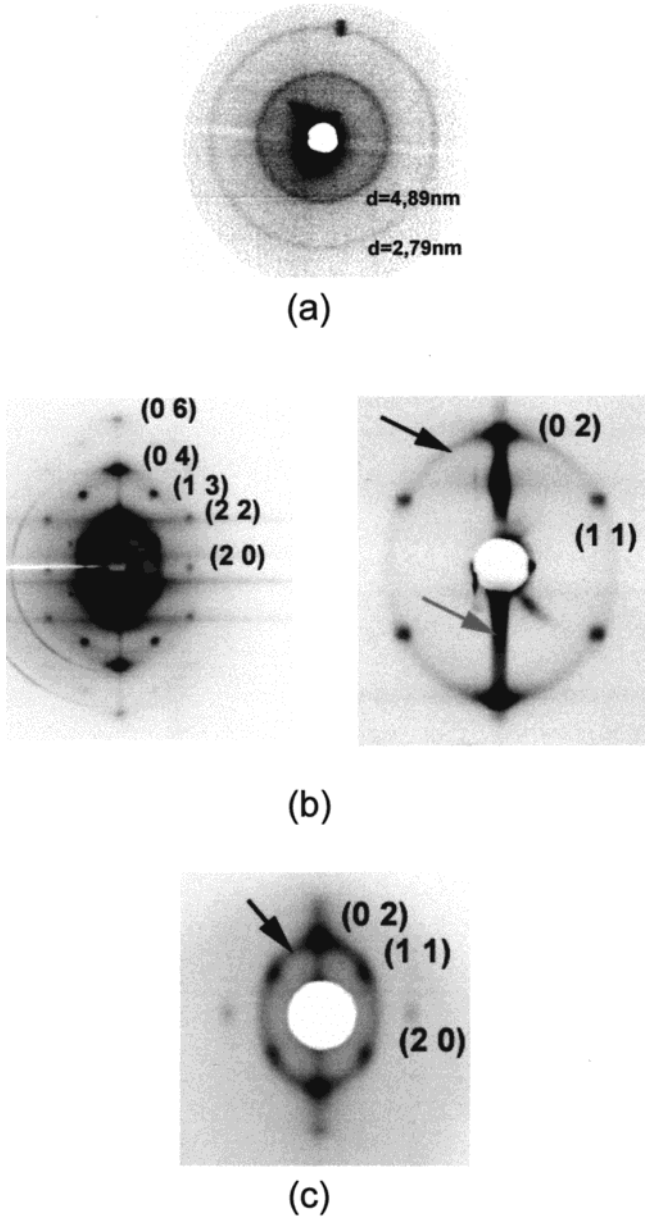

Figure 5. 2D X-ray scattering patterns for unseeded thin layers C: (a) normal incidence − 20 °C ($l_{sd} = 500$ mm; $t_e = 3$ h); (b) grazing incidence − 20 °C: left-side: $l_{sd} = 198$ mm; $t_e = 6$ h; right-side: $l_{sd} = 500$ mm; $t_e = 1$ h; and (c) grazing incidence − 450 °C ($l_{sd} = 218$ mm; $t_e = 30'$).

Table 1. Structural Parameters Deduced from the Analysis of Normal-Incidence Scattering Patterns for the C Samples

sample	inner scattering ring (nm)	outer scattering ring (nm)	position ratio
unseeded, 20 °C	4.89	2.79	1.75
unseeded, 450 °C	5.05	2.90	1.74
maghemite seeded, 450 °C	4.94	2.87	1.72
silica seeded, 450 °C	5.04	2.82	1.79

and that quite often important intensity changes are observed from one sample to another. The diffraction spots can again be indexed with a centered rectangular cell but with different parameters: $a = 5.80$ nm and $b = 7.06$ nm. The d spacing of the (0 2) reflection is 3.53 nm, in close agreement with the value found in $\theta/2\theta$ scan (3.58 nm). The elliptical diffusion is more clearly visible and is characterized by a higher eccentricity

Table 2. Structural Parameters Deduced from the Analysis of Grazing-Incidence Scattering Patterns for the C Samples

sample	*a* (nm)	*b* (nm)	short axis (nm)	large axis (nm)	eccentricity	$a\sqrt{3}/b$
unseeded, 20 °C	5.58	8.06	4.89	4.03	1.21	1.20
unseeded, 450 °C	5.80	7.06	5.05	3.53	1.43	1.42
maghemite seeded, 450 °C			4.94	3.53	1.40	
silica seeded, 450 °C			5.04	3.58	1.41	

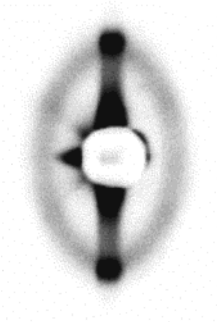

Figure 6. 2D X-ray pattern at grazing incidence for unseeded thin layer P (l_{sd} = 502 mm; t_e = 1 h).

(axes: 3.53 and 4.87 nm, respectively). Two rings are observed at 5.05 and 2.90 nm in normal incidence geometry.

Pluronic Based Sample. The scattering pattern presented in Figure 6 is taken in grazing incidence geometry and demonstrates that the observation of diffuse ellipses in mesoporous films is a more general phenomenon. The ellipse axes are 7.8 and 13.6 nm corresponding to an eccentricity of 1.74, higher than observed in CTAB-based samples (Table 2).

Discussion of the 2D X-ray Scattering. The unseeded layer C dried at 20 °C that presents the highest degree of organization is discussed first. As outlined before, domains with a cylindrical 2D hexagonal structure could be expected under the conditions utilized for film elaboration. It is well-known that the most dense lattice planes are preferentially oriented parallel to the surface as depicted in Figure 2 (notice the use of a centered rectangular cell for the hexagonal lattice with $b_0 = a_0\sqrt{3}$). The corresponding reciprocal lattice is also given in Figure 2. The observation of intense equatorial Bragg reflections in grazing incidence geometry indicates that most domains actually share this type of orientation. On the other hand the observation of homogeneous scattering in a normal incidence geometry reflects an absence of in-plane preferential orientation of the cylinder axes within the domains. This situation is schematically represented in Figure 7a. The reciprocal space associated with this organization is composed of coaxial circles as previously observed for hexagonal mesophases[17] (Figure 7b). Their intersection with the Ewald sphere is roughly visualized in Figures 7c and 7d for both normal and grazing configurations. In particular, it is clearly seen how sharp spots are obtained when these circles intersect the Ewald sphere in grazing incidence.

(17) Kékicheff, P.; Cabane, B. *Acta Crystallogr.* **1988**, *B44*, 395.

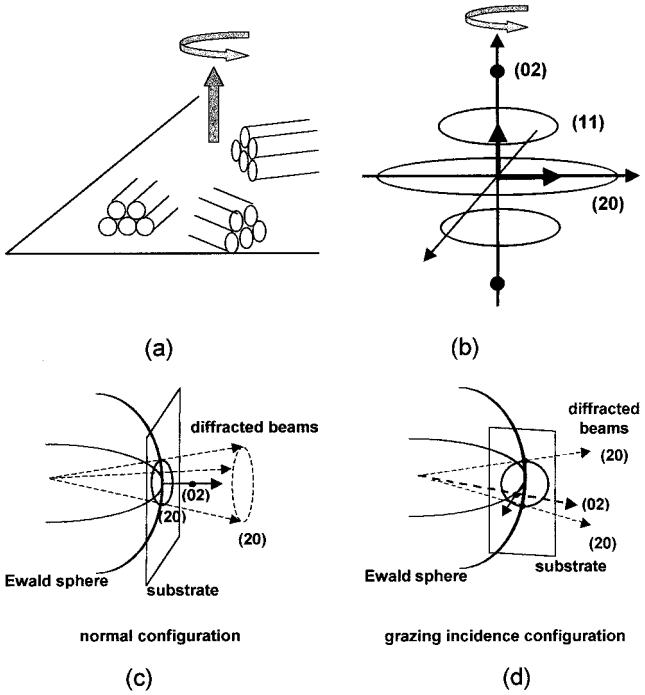

Figure 7. Schematic representation of the rotation of oriented domains along the $\vec{b}$ axis: (a) real space, (b) reciprocal space, (c) intersection with the reflection sphere in normal configuration, and (d) intersection with the reflection sphere in grazing configuration.

The next point to be addressed is the rectangular centered symmetry ($b/a = 1.44$) that is found instead of true hexagonal symmetry ($b_0/a_0 = \sqrt{3}$). This fact is due to shrinkage that occurs during solvent evaporation. It has been pointed out before that due to the film geometry, this phenomenon could be described as a constrained one-dimensional shrinkage.[18] It is to be expected that in-plane and out-of-plane parameters are differently affected. In these conditions, the flat-lying domains lose hexagonal symmetry while keeping rectangular symmetry. Domains which do not present this planar orientation should evolve toward oblique symmetry. Indeed, shrinkage is the key element to explain the elliptical diffusion observed on the scattering patterns and is now discussed in detail. Let us consider a domain with planar orientation: before shrinkage it presents a 2D hexagonal organization associated with the *p*6*mm* plane group. The different (*h k*) planes related by the symmetry elements of point group 6*mm* are equivalent and conventionally belong to the {*h k*} family of planes. It is for instance the case for (0 2), (1 1) and (1 $\bar{1}$) planes. The interplanar distance is similar and given by the relation: $1/d^2 = (3h^2 + k^2)/3a_0^2$ regardless of the *h k*. However, they present different orientations with respect to the substrate, and the interplanar distances follow a different evolution during shrinkage. This effect is now easily quantified knowing that the final state corresponds to a rectangular organization. For this purpose, it is more convenient to use $\vec{q}_{hk}$ reciprocal vectors which are recalled to be perpendicular to the (h k) planes, with $q_{hk} = 2\pi/d_{hk}$. In the hexagonal phase ($a = a_0$, $b = a_0\sqrt{3}$), the extremities of the vectors

(18) Brinker, C. J.; Scherer, G. W. *Sol−Gel Science: The Physics and Chemistry of Sol−Gel Processing*; Academic Press: San Diego, 1990.

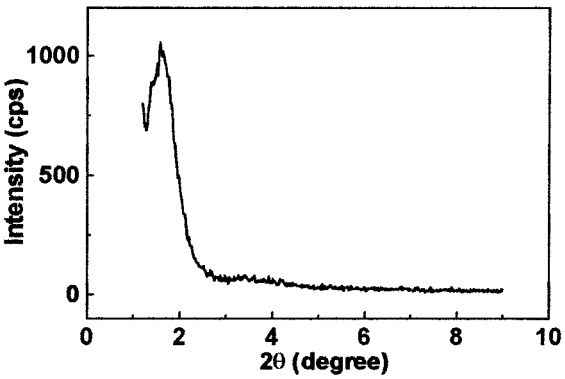

Figure 8. 1D classical X-ray diffraction pattern for a thick layer C treated at 450 °C.

associated with the planes of a $\{h\ k\}$ family are located on a circle. After shrinkage, in-plane and out-of-plane lattice parameters follow a different evolution ($a_0 \rightarrow a$ and $b_0 = a_0\sqrt{3} \rightarrow b$) and so do also the normal and in-plane components of the vector $\vec{q}_{hk}$:

$$q^{0\perp}{}_{hk} \rightarrow q^{\perp}{}_{hk} = q^{0\perp}{}_{hk}(b_0/b) \qquad (1a)$$

$$q^{0\parallel}{}_{hk} \rightarrow q^{\parallel}{}_{hk} = q^{0\parallel}{}_{hk}(a_0/a) \qquad (1b)$$

The extremities of the $\vec{q}_{hk}$ vectors are thus now located onto an ellipse of eccentricity $(b_0/b) \times (a/a_0) = a\sqrt{3}/b$. It is noticed that the elliptical eccentricity is independent of the starting $\{h\ k\}$ family. The absence of in-plane orientation for the planar domains is taken into account by averaging around the normal to the substrate yielding ellipsoids of revolution for the location of the vector extremities.

It can be assumed that some domains do not present any particular orientation: as quoted above, no specific symmetry elements should be preserved during shrinkage. However, we shall make the assumption that the evolution of the in-plane and normal components of a $\vec{q}_{hk}$ vector associated with $(h\ k)$ planes is still given by the relations in eq 1 derived for flat-lying domains. In other words the vector extremity will be located on one of the above-described ellipsoids. By considering all possible domain orientations, it results in a continuous description of the ellipsoids. Experimentally, the elliptical diffusion observed on both unseeded samples C clearly presents the above-described characteristics: it passes through the (2 0) and (1 1) reflections and the measured eccentricity is very close to the predicted value (see Table 2). The fact that no additional ellipses are observed for these particular samples is easily explained by (i) the structure factor of cylinders that steeply decreases with increasing scattering angle and (ii) the restricted number of domains that do not present planar orientation.

When comparing the data collected in Tables 1 and 2 for the unseeded samples C it is seen that the out-of-the-plane parameter b is reduced by roughly 13% during calcination, whereas the in-plane parameter a is slightly increased by 4% (near the error limit of the experiment). At the same time the in-plane elliptical short axis remains nearly unchanged. This last point is also observed for sample P exposed to calcination or to extraction by a solvent.[11] The in-plane parameters that correspond to lattice planes perpendicular to the substrate are thus only weakly affected by shrinkage: it justifies the term of constrained one-dimensional shrinkage and simultaneously explains why the d spacings of the two scattering rings observed in normal incidence are systematically in a ratio very close to $\sqrt{3}$ (see Table 1). The inner-ring radius corresponds to the d spacing for (0 2) lattice planes normal to the substrate. Similarly the outer ring is associated with (2 0) lattice planes normal to the substrate. Since the d spacings for planes presenting this orientation are only weakly affected by shrinkage, the ratio of their position must be close to the hexagonal value, i.e. $\sqrt{3}$. It accordingly follows that the value of the hexagonal parameter b_0 is approximately $2 \times 4.93 = 9.86$ nm at the moment of the film structuration. As a result a shrinkage of ~20% occurs

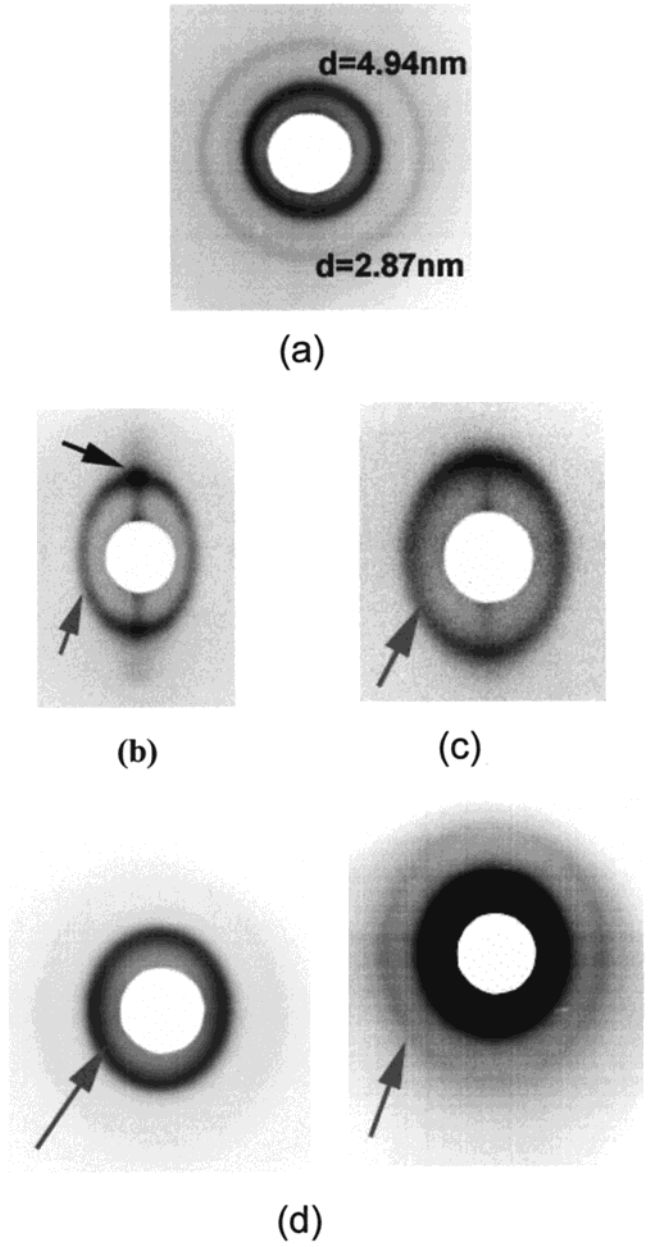

Figure 9. 2D X-ray patterns for seeded and calcined thin layers: (a) maghemite seeding − normal incidence (l_{sd} = 218 mm; t_e = 3 h); (b) maghemite seeding − grazing incidence (l_{sd} = 218 mm; t_e = 14′); (c) silica seeding − grazing incidence (l_{sd} = 218 mm; t_e = 20′); (d) silica seeding − incidence angle = 45° (l_{sd} = 218 mm; t_e = 15 h): left-hand and right-hand pictures correspond to the same pattern with a different gray scale.

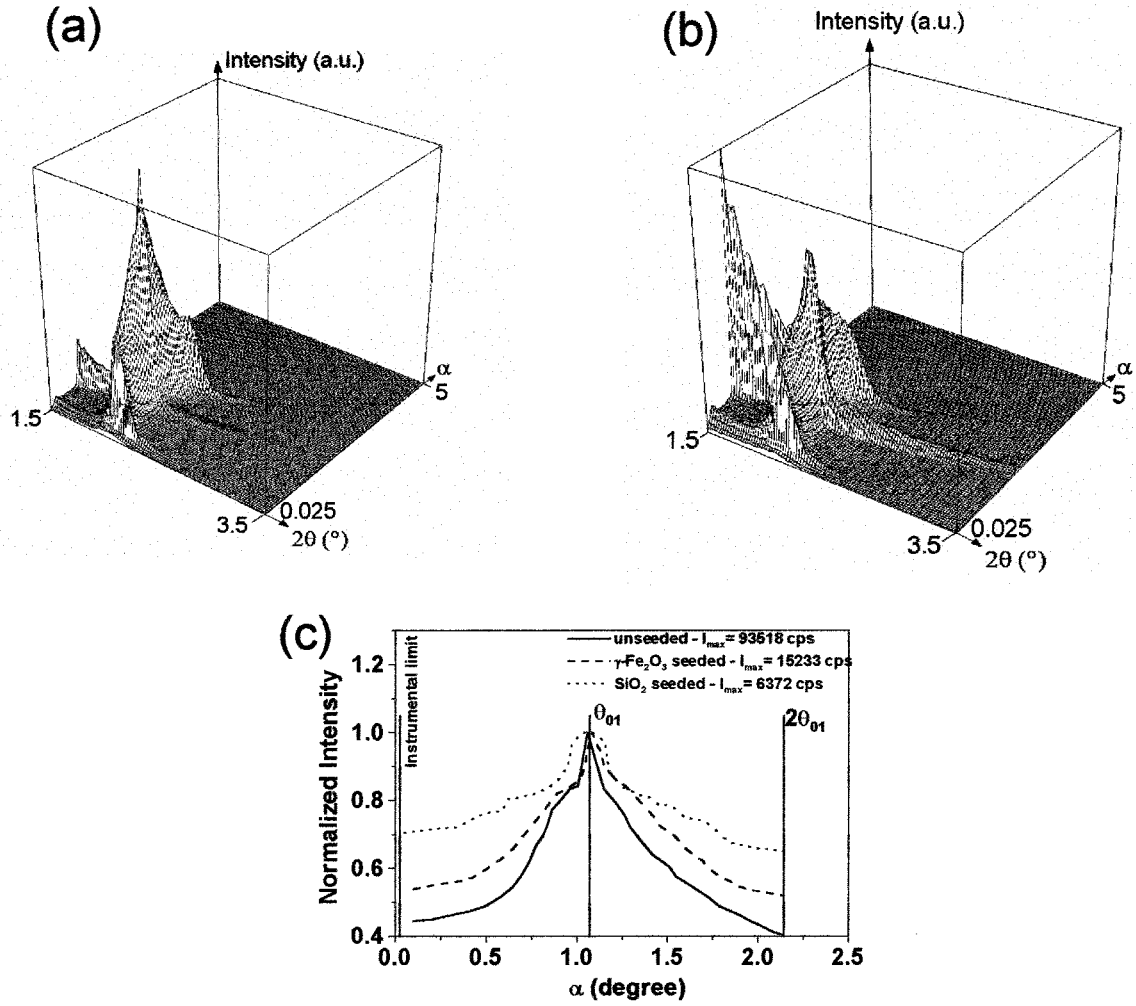

Figure 10. 1D classical X-ray diffraction as a function of incidence angle α for seeded thin layers C: (a) maghemite seeded − 20 °C, (b) silica seeded − 20 °C, and (c) variation of the intensity as a function of α at $2\theta = 2\theta_{01}$ for unseeded and seeded layers dried at 20 °C.

during solvent evaporation at room temperature.

The X-ray scattering pattern obtained from a cracked thick layer C prepared by pouring the gelling solution in a wide beaker presents a broad diffraction peak centered at 5.50 nm (Figure 8). The associated value for b_0 ($2 \times 5.50 = 11.0$ nm) is larger than before. This difference can be explained[10] by the significantly lower density of the silica walls in this last case due to different conditions of competitive drying and polymerization of the silica network.

Effect of the Nanoparticle Seeding on the Texture. To increase the pore accessibility and to improve the permeability of the final porous layers, it is interesting to be able to control the orientation of the ordered domains. Liu et al.[19] showed previously that nanoparticle seeding favors the formation of the templating mesophases in the synthesis medium. This seeding could promote a heterogeneous nucleation of the templating mesophase by creating additional interfaces inside the hybrid gelling solution. Moreover magnetic nanoparticles could be used to orient the mesophases under low magnetic field[20] as previously described in the case of ferrosmectics.[21]

We will first consider the results obtained from the 2D X-ray scattering analyses. These analyses were performed on thin layers calcined at 450 °C. For the maghemite seeded layers, the general aspect of the grazing-incidence pattern (Figure 9b) is quite different from the preceding ones: the diffuse ellipse (axes 3.53 and 4.94 nm, respectively) is now a prominent feature of the diagram. The only diffraction spots that remain visible are in the equatorial position (black arrow). Two homogeneous rings are observed at 4.94 and 2.87 nm in a normal incidence geometry (Figure 9a) and the diffracted ring at 4.94 nm is more intense than in the case of the unseeded samples. These results can be attributed to a first level of deorientation where some domains keep a flat-lying orientation.

For the silica seeded layers, the grazing-incidence pattern (Figure 9c) is closely related to Figure 9b. However no equatorial intensity enhancement is visible and the elliptical diffusion is perfectly homogeneous (axes 3.58 and 5.04 nm, respectively). Two rings are observed at 5.04 and 2.82 nm in normal incidence. The diagrams presented in Figure 9d are taken in an intermediate orientation with an incident angle of 45°. One observes an ellipse of lower eccentricity (left-hand

(19) Liu, J.; Kim, A. Y.; Virden, J. W.; Bunker, B. C. *Langmuir* **1995**, *11*, 659.

(20) Klotz, M.; Ayral, A.; Van der Lee, A.; Guizard, C.; Menager, C.; Cabuil, V. *Mater. Res. Soc. Symp. Proc.* **1999**, *576*, 247.

(21) Fabre, P.; Casagrande, C.; Veyssie, M.; Cabuil, V.; Massart, R. *Phys. Rev. Lett.* **1990**, *64*, 539.

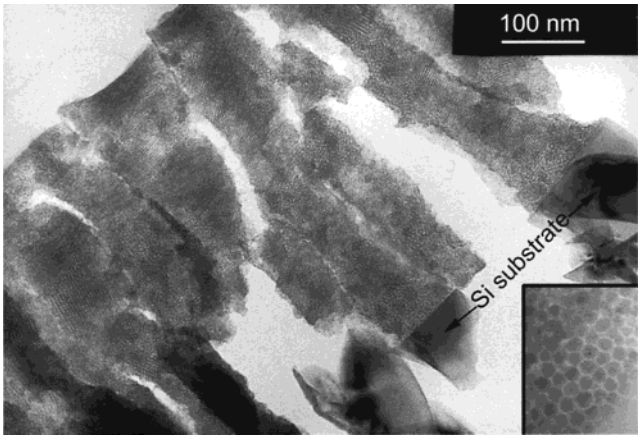

Figure 11. TEM cross section observation of a calcined silica seeded thin layer C. In this case, the silica nanoparticles (see inset: image from a previous TEM observation of the silica particles) cannot be easily observed due to the poor contrast difference with the matrix.

picture; axes 3.58 and 4.22 nm, respectively) that corresponds to an intermediate section of the diffuse ellipsoid (see discussion above). Thanks to the different choice of contrast used for the right-hand picture, an additional interesting scattering feature can be distinguished: it consists of a weak concentric ellipse indicated by a grey arrow. The complete disappearance of diffraction spots in the silica-doped sample and the observation of a very homogeneous ellipse clearly indicate that the domains are indeed randomly oriented in the film. This conclusion is supported by the observation of a second concentric diffuse ellipsoid in Figure 9d, since the scattered intensity is no longer concentrated in the strong diffraction spots. The observed differences between seeding with maghemite and silica particles could be mainly related to the difference of size between the used particles. The seeding density is the same in both cases.

The 1D X-ray diffraction evolution as a function of the incidence angle α and the transmission electron microscopy images are in line with the 2D X-ray scattering results. In Figure 10 the expected broadening of the peaks can be observed as well as a decrease of the intensity with increasing deorientation of the domains. The TEM image in Figure 11 nicely shows the random orientation in the case of the silica seeded layers.

Conclusion

This study has shown that the use of 2D imaging devices coupled to different scattering geometries is indispensable for a proper structural characterization of this type of highly textured silica thin layers. These materials are indeed closer to partially disordered single crystals than to "true" powders. It is unambiguously shown that in the absence of nanoparticle seeding the air−solution and substrate−solution interfaces generate a preferential orientation of the bidimensional structure parallel to the substrate surface. Drying and further thermal treatments induce an unidirectional shrinkage of the layers in a direction perpendicular to the interfaces: a compression of the 2D hexagonal arrangement of the micellar cylinders gives rise to a transition into a rectangular centered structure. Similar results are obtained with silica layers prepared using a block copolymer as surfactant. Nanoparticle seeding of the layers destroys the orientation of the $\vec{a}$ and $\vec{b}$ axes. This study is now extended to layers prepared by using alkyltrimethylammonium bromides, which are shorter than the cetyltrimethylammonium bromides used in this study. Dynamic characterization experiments of gas permeation on unseeded and seeded layers deposited on porous substrates are also in progress in order to investigate the effect of the orientation of the ordered domains on the permeability of the thin films.

Acknowledgment. The authors thank Dr. Marianne Clerc-Impéror (Laboratoire de Physique des Solides, Université de Paris-Sud, Orsay, France) for fruitful discussions. They are also greatly indebted to M. Lavergne who performed the electron micrographs in the Groupement Régional de Mesures Physiques (Université Pierre et Marie Curie−Paris VI, France).

CM991198T